J|A|C|S ARTICLES

Published on Web 06/24/2010

In Vitro and in Vivo Studies of FePt Nanoparticles for Dual Modal CT/MRI Molecular Imaging

Shang-Wei Chou,[†] Yu-Hong Shau,[‡] Ping-Ching Wu,[‡,§] Yu-Sang Yang,[‡,§] Dar-Bin Shieh,[*,‡,§,#,⊥] and Chia-Chun Chen[*,†,∥]

Department of Chemistry, National Taiwan Normal University, Taipei 11677, Taiwan., Institute of Oral Medicine and Department of Stomatology, National Cheng Kung University, Tainan 70101, Taiwan, Institute of Basic Medical Sciences, National Cheng Kung University, Tainan 70101, Taiwan, Advanced Optoelectronic Technology Center, National Cheng Kung University, Tainan 70101, Taiwan, Center for Micro/Nano Science and Technology, National Cheng Kung University, Tainan 70101, Taiwan, and Institute of Atomic and Molecular Sciences, Academia Sinica, Taipei 10617, Taiwan

Received April 24, 2010; E-mail: cjchen@ntnu.edu.tw; dshieh@mail.ncku.edu.tw

Abstract: The water-solvable FePt nanoparticles of 3, 6, and 12 nm in diameter (3 nm-, 6 nm-, and 12 nm-FePt) were synthesized and applied as a dual modality contrast agent for CT/MRI molecular imaging. These nanoparticles present excellent biocompatibility and hemocompatibility in all test concentrations for the imaging contrast. The biodistribution analysis revealed the highest serum concentration and circulation half-life for 12 nm-FePt, followed by 6 nm-FePt then 3 nm-FePt. Thus, the 3 nm-FePt showed higher brain concentrations. Anti-Her2 antibody conjugated FePt nanoparticles demonstrated molecular expression dependent CT/MRI dual imaging contrast effect in MBT2 cell line and its Her2/neu gene knock out counterpart. Selective contrast enhancement of Her2/neu overexpression cancer lesions in both CT and MRI was found in tumor bearing animal after tail vein injection of the nanoparticles. The 12 nm-FePt outperformed 3 nm-FePt in both imaging modalities. These results indicate the potential of FePt nanoparticles to serve as novel multimodal molecular imaging contrast agents in clinical settings.

Introduction

Recent advancement in nanomaterials preparation has brought about a significant impact for potential clinical applications in both diagnostics and therapeutics.[1−6] In particular, the medical imaging field has been empowered by nanoengineered smart targeting materials not only to present the disease loci, but also to reveal their clinical behavior at the molecular level.[7−9] Despite many studies have reported the use of nanoparticle-based imaging contrast agents for improved diagnostic imaging in a wide variety of modalities, the endogenous property of each modality may set the limit for the information those nanocontrast agent could provide. Therefore, it is conceivable that one single agent to provide imaging contrast in multiple imaging modalities would be of great value to offer more comprehensive diagnostic information and the dynamics of disease progression.

Computed tomography (CT) is one of the most routinely applied medical imaging modalities that give high-resolution 3D tomography information of the anatomic structure based on the differential X-ray absorption of the tissues and the lesion. Iodinated molecules and compounds with high X-ray absorption coefficient have been used for CT contrast enhancement for decades.[10−12] However, the renal toxicity and short imaging times due to rapid clearance by the kidney hampered their clinical applications.[13,14] Nanoparticle-based CT contrast agents such as polymer-coated bismuth sulfide (Bi_2S_3) nanoparticles and PEG-coated gold nanoparticles have been designed to overcome these disadvantages and to provide even better contrast effects.[15,16]

[†] Department of Chemistry, National Taiwan Normal University.
[‡] Institute of Oral Medicine and Department of Stomatology, National Cheng Kung University.
[§] Institute of Basic Medical Sciences, National Cheng Kung University.
[#] Advanced Optoelectronic Technology Center, National Cheng Kung University.
[⊥] Center for Micro/Nano Science and Technology, National Cheng Kung University.
[∥] Institute of Atomic and Molecular Sciences, Academia Sinica.

(1) Mulder, W. J. M.; Strijkers, G. J.; Van Tilborg, G. A. F.; Cormode, D. P.; Fayad, Z. A.; Nicolay, K. *Acc. Chem. Res.* **2009**, *42*, 904–914.
(2) Sperling, R. A.; Rivera gil, P.; Zhang, F.; Zanella, M.; Parak, W. J. *Chem. Soc. Rev.* **2008**, *37*, 1896–1908.
(3) Gao, J. H.; Gu, H. W.; Xu, B. *Acc. Chem. Res.* **2009**, *42*, 1097–1107.
(4) Kim, J.; Piao, Y.; Hyeon, T. *Chem. Soc. Rev.* **2009**, *38*, 372–390.
(5) Weissleder, R.; Mahmood, U. *Radiology* **2001**, *219*, 316–333.
(6) Cheon, J.; Lee, J. H. *Acc. Chem. Res.* **2008**, *41*, 1630–1640.
(7) Bryson, J. M.; Fichter, K. M.; Chu, W. J.; Lee, J. H.; Li, J.; Madsen, L. A.; McLendon, P. M.; Reineke, T. M. *Proc. Natl. Acad. Sci. U.S.A.* **2009**, *106*, 16913–16918.
(8) Atanasijevic, T.; Shusteff, M.; Fam, P.; Jasanoff, A. *Proc. Natl. Acad. Sci. U.S.A.* **2006**, *103*, 14707–14712.
(9) Simberg, D.; Duza, T.; Park, J. H.; Essler, M.; Pilch, J.; Zhang, L. L.; Derfus, A. M.; Yang, M.; Hoffman, R. M.; Bhatia, S.; Sailor, M. J.; Ruoslahti, E. *Proc. Natl. Acad. Sci. U.S.A.* **2007**, *104*, 932–936.
(10) Krause, W. *Adv. Drug Delivery Rev.* **1999**, *37*, 159–173.
(11) Kong, W. H.; Lee, W. J.; Cui, Z. Y.; Bae, K. H.; Park, T. G.; Kim, J. H.; Park, K.; Seo, S. W. *Biomaterials* **2007**, *28*, 5555–5561.
(12) deKrafft, K. E.; Xie, Z.; Cao, G.; Tran, S.; Ma, L.; Zhou, O. Z.; Lin, W. *Angew. Chem., Int. Ed.* **2009**, *48*, 9901–9904.
(13) Haller, C.; Hizoh, I. *Invest. Radiol.* **2004**, *39*, 149–154.
(14) Hizoh, I.; Haller, C. *Invest. Radiol.* **2002**, *37*, 428–434.
(15) Rabin, O.; Perez, J. M.; Grimm, J.; Wojtkiewicz, G.; Weissleder, R. *Nat. Mater.* **2006**, *5*, 118–122.

 10.1021/ja1035013

On the other hand, magnetic resonance imaging (MRI) is well-known to provide unsurpassed 3D soft tissue detail and functional information of the lesions. Because of its nonionizing radiation, high sensitivity to the distribution of water and other biomolecules, and the orientation of fine tissue structures, MRI has been applied in clinic for the diagnosis of many diseases.[17−19] Two major types of MRI image contrasts have been developed: the gadolinium (Gd^{3+})-based T_1 contrast agents and the superparamagnetic iron oxide nanoparticle based T_2 contrast agents.[20−24] Because of the high susceptibility and biocompatibility, these T_2 contrast agents provide a safe and strong negative contrast enhancement of the target lesion in MRI. A wide variety of iron oxide-based nanoparticles have been developed with different hydrodynamic sizes and surface modifications such as SiO_2, dextran, polyglutamic acid, and polyethylene glycol.[25−30] It has been shown that both size distribution and surface modifications may affect their biodistribution, metabolic clearance, and the MRI contrast effect.[30−33]

Despite both CT and MRI being essential medical imaging modalities and of significant clinical complementation, only few contrast agents have been developed recently with dual imaging contrast effect, which include the Gd-G8 dendrimer and the Gd chelated Au nanoparticles.[34,35] For the biocompatibility and practical utility, generally, these nanoagents were prepared through complex and excess procedures. As a result, to simplify the preparation of dual modality contrast agent is still a challenging work. To date, the synthesis of alloy nanoparticles provides us a new idea to overcome these tasks.

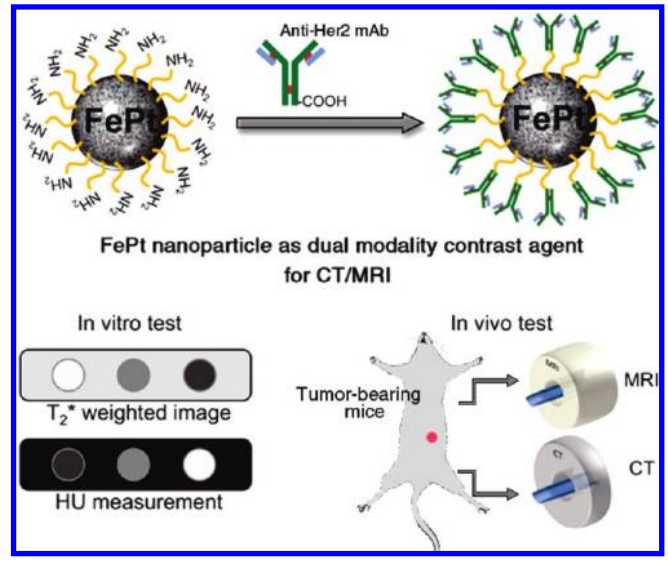

Figure 1. Schematic illustration showed that cysteamine capped FePt nanoparticles were prepared and then conjugated with anti-Her2 antibody. The FePt nanoparticles were used as a constrast agent for in vitro and in vivo MRI and CT evaluation for dual contrast enhancement.

FePt alloy nanoparticles (FePt nanoparticles) have been developed for high-density magnetic storage material due to their excellent stability and magnetic property.[3,36] The excellent superparamagnetic property and stability combined with the high X-ray absorption (X-ray absorption coefficient of Pt: 6.95 cm^2/g at 50 keV) make this alloy nanoparticle a potential MRI/CT dual imaging contrast agent.[37] Besides, the FePt nanoparticles may be synthesized with controllable size and shape and, thus, could be tailored for different clinical applications.[38,39] The surface modification methods of the FePt nanoparticles are similar to those well developed for gold nanoparticles commonly through thiol−metal bond.[3,40,41] Thus, the surface chemistry could be easily tuned for biological stealth and targeting functions.

In this work, the FePt nanoparticles with 3, 6, and 12 nm in diameter were synthesized and explored for their potentials as a dual modality contrast agent for CT and MRI (Figure 1). We used polyol method to synthesize these nanoparticles at high temperature and modify their surface with cysteamine to expose the amine group for further bioconjugation. A series of comprehensive evaluations were performed to characterize their morphology, size distribution, magnetic property, biocompatibility, hemocompatibility and biodistribution. Furthermore, the

(16) Kim, D.; Park, S.; Lee, J. H.; Jeong, Y. Y.; Jon, S. *J. Am. Chem. Soc.* **2007**, *129*, 7661–7665.
(17) Cheng, H. Y.; Nair, G.; Walker, T. A.; Kim, M. K.; Pardue, M. T.; Thule, P. M.; Olson, D. E.; Duong, T. Q. *Proc. Natl. Acad. Sci. U.S.A.* **2006**, *103*, 17525–17530.
(18) Wu, P. C.; Su, C. H.; Cheng, F. Y.; Weng, J. C.; Chen, J. H.; Yeh, C. S.; Shieh, D. B. *Oral Oncol.* **2007**, *2*, 156–156.
(19) McEvoy, L. K.; Fennema-Notestine, C.; Roddey, J. C.; Hagler, D. J.; Holland, D.; Karow, D. S.; Pung, C. J.; Brewer, J. B.; Dale, A. M.; Initia, A. D. N. *Radiology* **2009**, *251*, 195–205.
(20) Huh, Y. M.; Jun, Y. W.; Song, H. T.; Kim, S.; Choi, J. S.; Lee, J. H.; Yoon, S.; Kim, K. S.; Shin, J. S.; Suh, J. S.; Cheon, J. *J. Am. Chem. Soc.* **2005**, *127*, 12387–12391.
(21) Lim, Y. T.; Cho, M. Y.; Choi, B. S.; Lee, J. M.; Chung, B. H. *Chem. Commun.* **2008**, 4930–4932.
(22) Debouttiere, P. J.; Roux, S.; Vocanson, F.; Billotey, C.; Beuf, O.; Favre-Reguillon, A.; Lin, Y.; Pellet-Rostaing, S.; Lamartine, R.; Perriat, P.; Tillement, O. *Adv. Funct. Mater.* **2006**, *16*, 2330–2339.
(23) Caravan, P.; Ellison, J. J.; McMurry, T. J.; Lauffer, R. B. *Chem. Rev.* **1999**, *99*, 2293–2352.
(24) Wijaya, A.; Schaffer, S. B.; Pallares, I. G.; Hamad-Schifferli, K. *ACS Nano* **2009**, *3*, 80–86.
(25) Jeong, U.; Teng, X. W.; Wang, Y.; Yang, H.; Xia, Y. N. *Adv. Mater.* **2007**, *19*, 33–60.
(26) Taboada, E.; Solanas, R.; Rodríguez, E.; Weissleder, R.; A., R. *Adv. Funct. Mater.* **2009**, *19*, 2319–2324.
(27) Na, H. B.; Song, I. C.; Hyeon, T. *Adv. Mater.* **2009**, *21*, 2133–2148.
(28) Moffat, B. A.; Reddy, G. R.; McConville, P.; Hall, D. E.; Chenevert, T. L.; Kopelman, R. R.; Philbert, M.; Weissleder, R.; Rehemtulla, A.; Ross, B. D. *Mol. Imaging* **2003**, *2*, 324–332.
(29) Shi, X. Y.; Wang, S. H.; Swanson, S. D.; Ge, S.; Cao, Z. Y.; Van Antwerp, M. E.; Landmark, K. J.; Baker, J. R. *Adv. Mater.* **2008**, *20*, 1671–1678.
(30) Tromsdorf, U. I.; Bigall, N. C.; Kaul, M. G.; Bruns, O. T.; Nikolic, M. S.; Mollwitz, B.; Sperling, R. A.; Reimer, R.; Hohenberg, H.; Parak, W. J.; Forster, S.; Beisiegel, U.; Adam, G.; Weller, H. *Nano Lett.* **2007**, *7*, 2422–2427.
(31) Song, H. T.; Choi, J. S.; Huh, Y. M.; Kim, S.; Jun, Y. W.; Suh, J. S.; Cheon, J. *J. Am. Chem. Soc.* **2005**, *127*, 9992–9993.
(32) Wu, P. C.; Su, C. H.; Cheng, F. Y.; Weng, J. C.; Chen, J. H.; Tsai, T. L.; Yeh, C. S.; Su, W. C.; Hwu, J. R.; Tzeng, Y.; Shieh, D. B. *Bioconjugate Chem.* **2008**, *19*, 1972–1979.
(33) Su, C. H.; Sheu, H. S.; Lin, C. Y.; Huang, C. C.; Lo, Y. W.; Pu, Y. C.; Weng, J. C.; Shieh, D. B.; Chen, J. H.; Yeh, C. S. *J. Am. Chem. Soc.* **2007**, *129*, 2139–2146.
(34) Regino, C. A. S.; Walbridge, S.; Bernardo, M.; Wong, K. J.; Johnson, D.; Lonser, R.; Oldfield, E. H.; Choyke, P. L.; Brechbiel, M. W. *Contrast Media Mol. Imaging* **2008**, *3*, 2–8.
(35) Alric, C.; Taleb, J.; Le Duc, G.; Mandon, C.; Billotey, C.; Le Meur-Herland, A.; Brochard, T.; Vocanson, F.; Janier, M.; Perriat, P.; Roux, S.; Tillement, O. *J. Am. Chem. Soc.* **2008**, *130*, 5908–5915.
(36) Sun, S. H. *Adv. Mater.* **2006**, *18*, 393–403.
(37) Page for X-Ray Mass Attenuation Coefficients for Pt. http://physics.nist.gov/PhysRefData/XrayMassCoef/ElemTab/z78.html.
(38) Chou, S. W.; Zhu, C. L.; Neeleshwar, S.; Chen, C. L.; Chen, Y. Y.; Chen, C. C. *Chem. Mater.* **2009**, *21*, 4955–4961.
(39) Chen, M.; Liu, J. P.; Sun, S. H. *J. Am. Chem. Soc.* **2004**, *126*, 8394–8395.
(40) Gu, H. W.; Ho, P. L.; Tsang, K. W. T.; Wang, L.; Xu, B. *J. Am. Chem. Soc.* **2003**, *125*, 15702–15703.
(41) Xu, C. J.; Xu, K. M.; Gu, H. W.; Zhong, X. F.; Guo, Z. H.; Zheng, R. K.; Zhang, X. X.; Xu, B. *J. Am. Chem. Soc.* **2004**, *126*, 3392–3393.

contrast enhancement of dual modality CT/MRI molecular imaging was evaluated in both in vitro and in vivo models using paired tumor lines with modulated Her2 oncogene expression levels through stably transfected siRNA against Her2 oncogene. These results provide an insight for further clinical translational development of this new type of nanocontrast agent in multimodal medical imaging applications.

Experimental Section

Materials. Platinum acetylacetonate ($Pt(acac)_2$, ACROS, 97%) and iron pentacarbonyl ($Fe(CO)_5$, Aldrich, 99.99%) 1,2-hexadecanediol (Aldrich, 90%), dioctyl ether (ACROS, 90%), oleyl amine (Aldrich, 70%), oleic acid (Aldrich, 90%), cysteamine (Sigma, 95%).

Synthesis of 3 to 4 nm FePt Nanoparticles. $Pt(acac)_2$ (97 mg), 1,2-hexadecandiol (195 mg), and dioctyl ether (10 mL) were mixed and heated to 100 °C under N_2 for 10 min. $Fe(CO)_5$ (66 μL), oleyl amine (80 μL), and oleic acid (80 μL) were injected at 100 °C. The reaction mixture was heated to 297 °C at heating rate of 15 °C/min. After 30 min, the heating source was removed and the product was cooled to the room temperature. The product was precipitated by adding ethanol and separated by centrifugation.

Synthesis of 6 to 7 nm FePt Nanoparticles. $Pt(acac)_2$ (97 mg), dioctyl ether (4 mL), $Fe(CO)_5$ (66 μL), 1,2-hexadecandiol (195 mg), oleyl amine (100 μL), and oleic acid (100 μL) were mixed under nitrogen. The reaction mixture was heated to 240 °C at heating rate of 15 °C/min. After 30 min, the heating mantle was removed and then the product was cooled to the room temperature. The particles were collected by centrifugation.

Synthesis of 12 to 13 nm FePt Nanoparticles. The procedure was referred to the previous publication.[38] The synthesis was as following: $Pt(acac)_2$ (195 mg), 1,2-hexadecandiol (1.05 g), dioctyl ether (4 mL), $Fe(CO)_5$ (66 μL), oleyl amine (4 mL), and oleic acid (4 mL) were mixed under N_2 and then heated to 240 °C at heating rate of 15 °C/min. The mixture was kept at 240 °C for 60 min. Then, the heating mantle was removed and the reaction mixture was cooled to room temperature. The final product was separated by addition of ethanol followed by centrifugation. Overall, the final product was stored in hexane or toluene.

Ligand Exchange. Dry FePt nanoparticles (100 mg) were dispersed in ethanol by sonication. Cysteamine (~1 g) was added and dissolved into this solution at room temperature. This mixture was sonicated at 40−50 °C overnight. Then, the sample was washed to remove ligand adsorbed on particles by ethanol. Finally, the modified particles were collected and stored in the bottle filled with N_2.

The FePt Nanoparticles Conjugated with Anti-Her2 Antibody. The FePt nanoparticles with amine group were incubated with Ethyl-3-[3-dimethylaminopropyl] carbodiimide hydrochloride (EDC) and mouse anti-Her2 antibodies. The solutions were stirred at 4 °C for 1 h. The pallets were centrifuged at 13000 rpm for 15 min and washed in phosphate-buffered saline (PBS) twice before the next steps.

Characterization of FePt Nanoparticles. The work of transmission electron microscope (TEM) and X-ray energy-dispersive spectroscopy (EDX) was carried out on a Philips/FEI Tecnai 20 G2 S-Twin transmission electron microscope. A small amount of sample was deposited in toluene. A drop of solution was placed on an amorphous carbon membrane supported by a copper grid. The particles were determined at magnification of 200k. Powder X-ray diffraction data was collected on a Bruker D8 Advance diffractometer. The FePt powder was placed on amorphous Si wafer and the workup procedure was carried out with Cu Kα radiation (λ = 1.54178 Å). Magnetic measurements were performed by superconducting quantum interference device (SQUID) magnetometer (MPMS, Quantum Design). The measurements were recorded between −10000 and 10000 Oe at 300 K. The ligand attachment of FePt nanoparticles was characterized by FTIR spectrophotometer (Thermo Nicloe FT-IR) with a resolution of 2 cm^{-1}.

Cell Culture. Human oral epidermoid carcinoma cell line (OECM1) was maintained in RPMI-1640 medium supplemented with 10% (v/v) fetal bovine serum. Vero cells were maintained in DMEM medium containing 10% fetal bovine serum (FBS), 2 mM L-glutamine, and 50 mg/mL gentamicin. The murine MBT2 cell line derived from a carcinogen-induced bladder tumor in C3H/HeN mice was obtained from American Type Culture Collection (ATCC, Manassas, VA). Cells were maintained in DMEM supplemented with 10% FBS, 25 mM *N*-2-hydroxyethylpiperazine-*N*-2- ethanesulfonic acid (HEPES), 2 mM L-glutamine, and 1 mM sodium pyruvate. All the cell lines were maintained in a 37 °C incubator with a humidified environment of 5% CO_2 in the air. Medium was changed every 2 days.

In Vitro Cytotoxicity Assay (MTT Assay) and Hemolysis Assay. A total of 5×10^3 Vero cells/well were seeded in 96-well plates with DMEM supplemented with 10% FBS, 2 mM L-glutamine, and 50 mg/mL gentamicin. After 24 h, various sizes (3, 6, and 12 nm) and serial 10-fold dilutions of the FePt nanoparticles were added to cells with final concentrations ranging from 0.01 to 100 mM (iron concentration) for an additional 24 h. Cell viability was detected using the 5-dimethylthiazol-2-yl-2, 5-diphenyl tetrazolium bromide (MTT) assay. After the cells were treated with MTT and incubated at 37 °C for 4 h, the purple formazan in supernatant was quantified by measuring 595 nm absorbance using a spectrophotometer.

Hemolysis assay was performed using human whole blood from a healthy donor with informed consent following IRB guidelines. The FePt nanoparticles were added to the 200 μL human whole blood stored in the Vacutainer (BD, Inc.) containing 24 IU sodium heparin to the final concentrations in the range of 0.0001−100 mM (iron concentration). The tubes were gently mixed in a rotary shaker, and then incubated for 4 h at 37 °C. The specimens were then centrifuged at 1200 rpm for 10 min to collect the serum. The serum was further centrifuged at 13000 rpm for 15 min to remove the FePt nanoparticles and the supernatant was analyzed for the presence of the hemoglobin by specific 545 nm spectrophotometric absorption.

Organ Distribution. Six-week old male C3H/HeN mice purchased from animal center of NCKU were anesthetized by 40 mg/kg pantothol and were injected FePt nanoparticles through tail vein at dose of 5 mg/kg for 12, 24, 48, 96, and 168 h before being sacrificed. After saline perfusion, organs such as the brain, heart, lung, spleen, liver, kidney, testis, and blood were collected and ground with nitro-hydrochloride acid. After filtration, the solution samples were analyzed using a flame atomic absorption spectrometer (UNICAM solar M6 series).

In Vitro MRI and CT Image. An array of Eppendorf tubes containing different concentrations of the FePt nanopartiles (0.01−100 mM Fe) and the PBS control was prepared for MRI and CT contrast imaging. The magnetic resonance imaging (MRI) for in vitro study was performed by the following sequences: T_2-weighted three-dimensional fast-field echo sequences (repetition time in ms/echo time in ms/flip angle/number of acquisitions, 550/15/15°/3), field of view of 140 × 100 mm, a matrix of 256 × 196 pixels and a slice thickness of 1.4 mm. The computed tomography (CT) data were acquired using a GE Light Speed VCT 64-detector CT. Imaging parameters were as follows: slice thickness, 0.625 mm; 120 kVp, 30 mA; field of view, 512 × 512, gantry rotation time, 0.4 s; table speed, 40 mm/rotation.

In Vitro Targeting Molecular Imaging of Her2 Expression. A total of 10^7 MBT2 and MBT2 Her2 knock-down cells were fixed with 4% paraformaldehyde and resuspended into a 15 mL tube, then incubated with anti-Her2 antibody tagged FePt nanoparticles with diameters of 3 and 12 nm and the control nanoparticles (without tagged antibody) in final iron concentration of 1 mM. After 4 h incubation, 10^7 cells in each group were placed in an Eppendorf tube array and analyzed for the contrast effect in an MR imager.

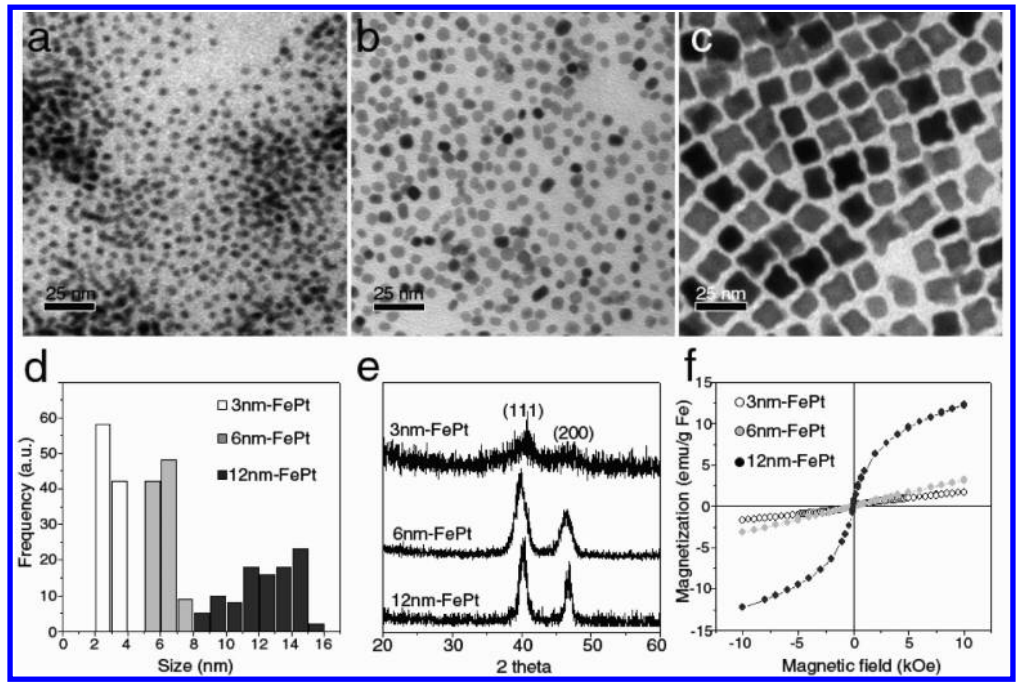

Figure 2. (a−c) TEM images of FePt nanoparticles with three different sizes. (d) The size distributions of the FePt nanoparticles acquired from 100 nanoparticles for each sample. (e) The XRD scans of FePt nanoparticles. (f) The hysteresis loops of FePt nanoparticles recorded between −10000 and 10000 Oe at 300 K. The magnetic hysteresis loops showed that the net magnetization of all samples was zero in the absence of the external field.

The following pulse sequences were used: T_2-weighted sequence, fast spin echo with TR = 550, TE = 15, echo train length (ET) = 10 ms. The array was then subjected to CT scan following parameters described in the in vitro imaging protocol.

In Vivo Targeting Molecular Imaging of Her2 Expression. The in vivo imaging was performed using mice with transplanted MBT2 tumor. The male C3H/HeN, 6−8 weeks old mice were provided by National Cheng Kung University Laboratory Animal Center (Tainan, Taiwan). MBT2 tumor lesions were established by subcutaneous dorsal flank injection of 10^7 tumor cells in 100 μL normal saline using a 27-gauge needle. Visible tumor was normally observed 1 week after implantation. Animals were anesthetized using 2% isoflurane (Abbott Laboratories, Abbott Park, IL) mixed with 100% O_2 delivered using a veterinary anesthesia delivery system (ADS 1000; Engler Engineering Corp., Hialeah, FL). The tumor lesions were then subject to the two imaging modality analysis after tail vein injection of anti-Her2 antibody tagged FePt nanoparticles (5 mg Fe/kg). The images were taken at a time sequence from 0−24 h using T_2-weighted MR acquisition sequence with the following parameters: fast spin echo with TR/TE = 3000 ms/99.7 ms, ET = 10 ms. The signal intensity of tissue in each test was determined by standard region-of-interest measurements of cross-sectional image of the tissue using the provided image quantification software. The in vivo microcomputed tomography analysis (Skyscan 1076 X-ray Microtomograph, Skyscan, Aartselaar, Belgium) was then performed using microfocused X-ray source (50 keV/200 Ua) illumination; each image acquisition was performed when rotated one step (1°) through 360°. The images were processed for cross sections by reconstruction using NRecon (Skyscan) software.

Results and Discussion

Characterization of FePt Nanoparticles. The TEM images of FePt nanoparticles were shown in Figure 2a−c with the sizes of 3.58 ± 0.34, 6.12 ± 0.63, and 12.80 ± 1.76 nm, respectively. Their size distribution (Figure 2d) was obtained from averaging the sizes of 100 nanoparticles. The FePt nanoaprticles in Figure 2a,b were in a nearly spherical shape (a cuboctahedron structure under HRTEM), while the large FePt nanoparticles presented a cubic-like shape (Figure 2c).[38] The EDX analysis of the samples in Figure 2a−c revealed that the alloying compositions of the three samples were $Fe_{58}Pt_{42}$, $Fe_{51}Pt_{49}$, and $Fe_{33}Pt_{67}$, respectively. The typical XRD spectra in Figure 2e showed the strongest peaks of the (111) and the (200) facet of a face-centered cubic (fcc) structure. Further, as the broader XRD patterns usually suggest smaller particle size,[42] the XRD patterns were consistent with the size of the nanoparticles observed in the TEM images. The size and shape of FePt nanoparticles remained unchanged in TEM measurements after the nanoparticle surface was capped with cysteamine or anti-Her2 antibody. The ligand exchanges of FePt nanoparticles with cysteamine and anti-Her2 antibody were confirmed from the FTIR measurements (in Supporting Information). In particular, the characteristic bands of C−N, C−O, and C−H from the anti-Her2 antibody were clearly observed after the antibody was successfully conjugated onto the surface of FePt nanoparticles. The magnetic hysteresis loops (Figure 2f) showed that all samples exhibited superparamagnetic behavior at 300 K. The saturated mass magnetizations (M_s) at 300 K are in the sequence: $M_{s\ FePt(12\ nm)}$ (12.3 emu/g Fe) > $M_{s\ FePt(6\ nm)}$ (3.2 emu/g Fe) > $M_{s\ FePt(3\ nm)}$ (1.7 emu/g Fe). The results indicated that mass magnetization was proportional to their sizes.[43] These were consistent with previous studies that magnetic properties of FePt octapod, cuboctahedron and nanocube exhibited strong dependency

(42) Klug, H. P.; Alexander, L. E. *X-ray Diffraction Procedures for Polycrystalline and Amorphous Materials*; Wiley: New York, 1962.
(43) Park, J. H.; Lee, E.; Hwang, N. M.; Kang, M. S.; Kim, S. C.; Hwang, Y.; Park, J. G.; Noh, H. J.; Kini, J. Y.; Park, J. H.; Hyeon, T. *Angew. Chem., Int. Ed.* **2005**, *44*, 2872–2877.

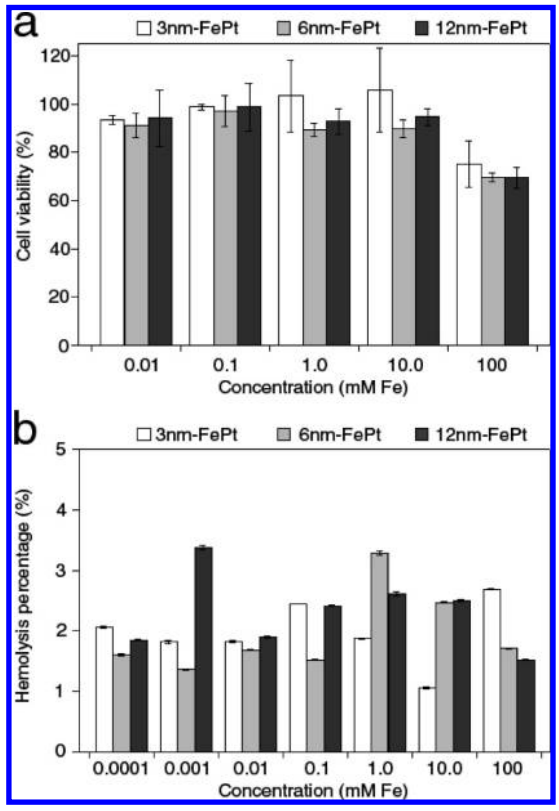

Figure 3. (a) The in vitro cytotoxicity evaluated by MTT assay in the range of 0.01−100 mM Fe of 3 nm-, 6 nm-, and 12 nm-FePt. (b) Hemolysis test at various Fe concentrations (0.0001−100 mM Fe) of 3 nm-, 6 nm-, and 12 nm-FePt.

on their size and shape.[38,44] In addition, the effect of alloying component in mass magnetization was not obvious in this work.

Biocompatibility. The in vitro cytotoxicity of FePt nanoparticles was evaluated in a Vero cell line by MTT assay. The water-solvable cysteamine capped FePt nanoparticles of 3, 6, and 12 nm in diameters (3 nm-, 6 nm-, and 12 nm-FePt, respectively) were tested over a dosage range of 0.01−100 mM of Fe concentration. The MTT assay (Figure 3a) showed no significant cytotoxic response (the cell viability >90%) detected at concentration below 10 mM after 24 h of exposure. Futher, at the highest concentration of 100 mM, the cell viability was still up to 75%. There are no significant difference in the cell viability as affected by the particle size. In hemolysis test, the free hemoglobin in the serum from lysed erythrocytes was detected by OD_{545} to calculate the percentage of hemolysis upon exposure to various sizes and concentrations of FePt nanoparticles. The results (Figure 3b) indicated that no significant hemolysis (<5%) occurred in all FePt nanoparticles at various concentrations. Our results revealed the high cell viability and low hemolysis for FePt nanoparticles with different sizes and suggest their excellent in vitro biocompatibility.

Biodistribution. We further analyzed the effect of particle size to their biological distribution in 6-week old male C3H/HeN mice (Figure 4). The results indicate that most of the nanoparticles were cleared from the major organs after 1 week (168 h). Larger particle size has higher serum concentration and

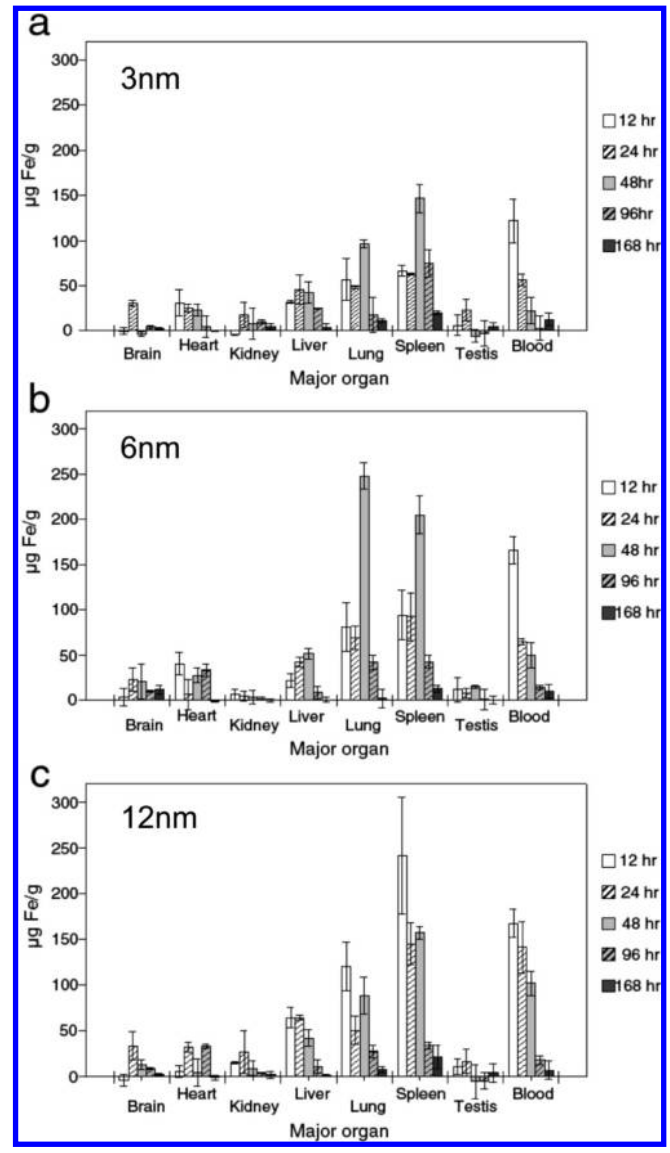

Figure 4. Biodistribution of (a) 3 nm-FePt, (b) 6 nm-FePt, and (c) 12 nm-FePt, in the major organs of the C3H/HeN mice including brain, heart, kidney, liver, lung, spleen, testis, and blood. The data was recorded from whole organ taken at indicated times after injection.

longer serum half-life, and all three sizes of particles approach the background levels after 96 h. There are 102.2 μg/g of 12 nm-FePt in the serum 48 h after injection, while only 22.2 μg/g of the 3 nm-FePt and 49.6 μg/g of the 6 nm-FePt were detected at the same time point. The nanoparticles were mainly accumulated in the spleen followed by lung and liver and were gradually cleared from these organs with time. The 12 nm-FePt reached the plateau concentrations in these organs at 12 h after injection, while it was 48 h for the 3 nm- and 6 nm-FePt. The highest tissue concentrations of the nanoparticles in the spleen and lung for 12 nm-FePt were 241.5 and 120.4 μg/g, while they were 204.9 and 247.9 μg/g for 6 nm-FePt. The plateau concentrations for the 3 nm-FePt in the two organs were 146.6 μg/g in the spleen and 96.5 μg/g in the lung at 48 h. The 6 nm-FePt presented the lowest nonspecific hepatic uptake. We also detected transient accumulation of the nanoparticles in the brain at 24 h for all three particle-sizes. The 3 nm-FePt has the highest brain concentration consistent with the reported size limit of the blood−brain barrier.

(44) Nandwana, V.; Elkins, K. E.; Poudyal, N.; Chaubey, G. S.; Yano, K.; Liu, J. P. *J. Phys. Chem. C* **2007**, *111*, 4185–4189.

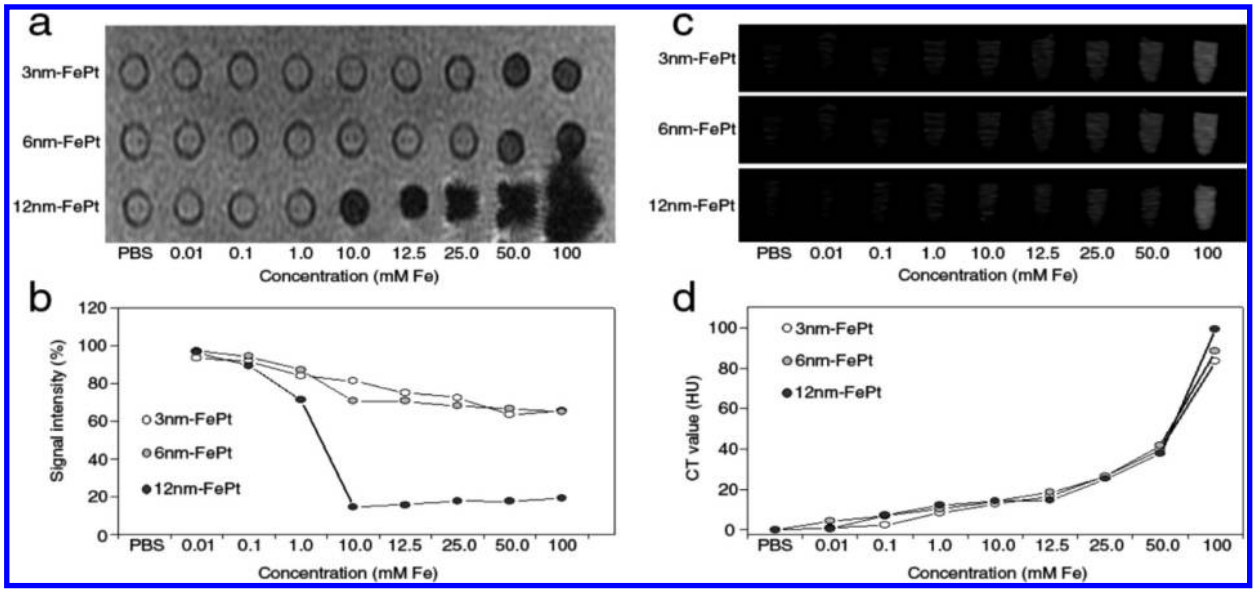

Figure 5. (a) The effective T_2*-weighted images of 3 nm-, 6 nm-, and 12 nm-FePt within a range of 0−100 mM Fe. (b) Quantitative analysis of the T_2* signal intensity normalized by that of PBS solution was illustrated for the three sizes of nanoparticles. (c) The in vitro CT imaging of 3 nm-, 6 nm- and 12 nm-FePt in the same dosage range. (d) The measured CT value of the nanoparticles.

Most previous reports agreed that particle size below 10 nm could permeate the blood−brain barrier, although some reported that 50 nm gold particles may also be detected in the brain after intravenous injection.[45] This may help to explain the presence of FePt nanoparticles in the brain and the inverse correlation between particle size and the plateau amount of accumulation. As all the three different nanoparticles have the same native surface of amine group, the major factor governing the difference in their biodistribution should mostly be related to the size and morphology effect. However, complicated multiple factors may affect the dynamics in the entrance, adhesion, retention and processing, and clearance of nanoparticles in different tissues.[46,47] It is not clear at this moment the mechanism at molecular and tissue level underlying the differential biodistribution affected by the particle sizes of FePt nanoparticles. We did expect that a homeostasis in the entrance, trafficking and clearance of nanoparticles in the organs must play an important role. Further investigation using high-resolution TEM and molecular biology approaches are warranted. Overall, combining the biocompatibility, hemocompatibility and the biodistribution results, the FePt nanoparticles could potentially serve the in vivo applications.

In Vitro MR and CT Imaging. The in vitro T_2 and T_2* weighted imaging for 3 nm-, 6 nm-, and 12 nm-FePt were examined at various Fe concentrations. Figure 5a revealed the results (T_2* sequence) within the range of 0.01−100 mM Fe in PBS in a 1.5 T MR imager. The significant dose-dependent inverse MR image contrast was observed in all three arrays (Figure 5a). The calculated intensity of each pellet was referred to that of PBS pellet and the normalized results were plotted in Figure 5b. The 12 nm-FePt array presented the most effective negative MR contrast and the signal intensity decreased by 86% at the low concentration of 1 mM Fe. The 3 nm- and 6 nm-FePt array showed detectable image darkening by ∼28% for 3 nm-FePt and ∼33% for 6 nm-FePt at 25 mM Fe. Overall, 12 nm-FePt exerted the best inverse contrast effect in the in vitro experiment in a dose-dependent manner. In comparison with the image contrast effect of the commercial contrast agent (Resovist), the concentration required for the current 12 nm-FePt nanoparticles to present significant image contrast is much higher in a 3T MRI. However, the hydrodynamic size of Resovist is around 60 nm that limit their further development for in vivo molecular imaging. Nevertheless, further improvement of the contrast effect of the FePt nanoparticles by such as alloy composition and surface modification is required for optimal MRI contrast performance.

The in vitro CT imaging of the tube array was illustrated in Figure 5c. As expected, the scans demonstrated positive contrast enhancement in a dose-dependent manner. Appreciable enhancement for CT contrast was observed at 1 mM Fe for all three sizes of nanoparticles. The calculated CT signal contrast intensities within the range of 0.01−100 mM Fe was plotted in Figure 5d. The CT signal of 12 nm-FePt at 100 mM Fe (corresponding to 44.7 mg FePt/mL) exhibited the equivalent ability of CT contrast as 48.4 mg/mL of the popular iodine-containing agent.[16,48] In other words, the contrast effect of 12 nm-FePt was about equal to that of the current iodine-containing agent at the same concentration. Most worthily, according to the above calculation, the contrast effect of 3 nm- and 6 nm-FePt was approximately 2-fold higher than that of current iodine-containing agent at the same concentration.[48]

According to these results, FePt nanoparticles with fcc structure enhanced shortening T_2 of the proton relaxation due

(45) Sonavane, G.; Tomoda, K.; Makino, K. *Colloid Surf., B* **2008**, *66*, 274–280.
(46) Chouly, C.; Pouliquen, D.; Lucet, I.; Jeune, J. J.; Jallet, P. *J. Microencapsulation* **1996**, *13*, 245–255.
(47) Garnett, M. C.; Kallinteri, P. *Occup. Med.* **2006**, *56*, 307–311.
(48) On the basis of the EDX results, the weight concentration of FePt nanoparticles at various Fe concentrations is calculated. For example, the alloy composition of 12 nm-FePt is $Fe_{33}Pt_{67}$. As 12 nm-FePt is at 100 mM Fe, the Fe weight concentration is 5.2 mg/mL and the Pt weight concentration is approximately 39.5 mg/mL. As a result, the weight concentration of 3 nm-FePt at 100 mM Fe is corresponding to 19.3 mg/mL and the weight concentration of 6 nm-FePt at 100 mM Fe is corresponding to 23.9 mg/mL.

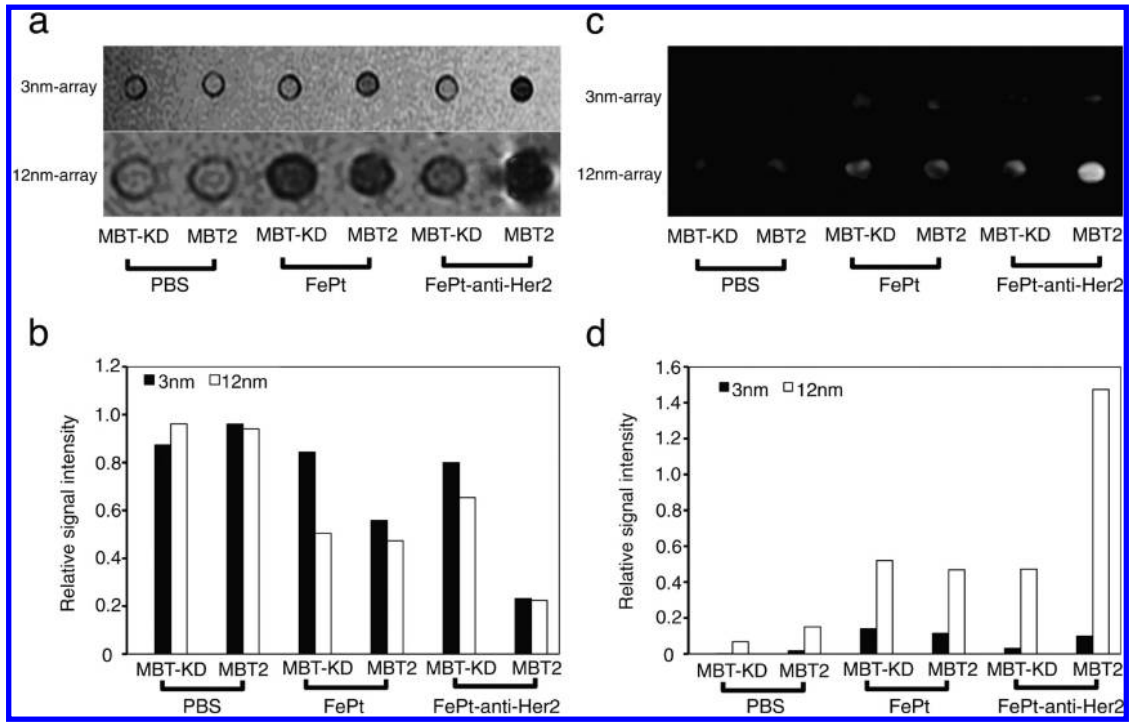

Figure 6. (a) The T_2*-weighted MR images of the cell pellets, including MBT2 Her2/neu knock-down cell (MBT-KD) and MBT2 cell (MBT2), targeted by the 3 nm-FePt, 3 nm-FePt−anti-Her2, 12 nm-FePt, and 12 nm-FePt−anti-Her2 at 1 mM Fe; the first two pellets are the untreated cell as the baseline control. (b) The MR signal intensity normalized by that of the cell pellets in PBS solution was illustrated. (c) The CT images of the same cell pellets array. (d) The CT signal intensity of the same cell pellets array.

to their superparamagnetic property while the high X-ray absorption coefficient (6.95 cm^2/g at 50 keV for Pt component) enables their efficient CT contrast enhancement. The size-dependent relationship in mass magnetization and X-ray absorption reflected the results of in vitro MR imaging and CT contrast.[49] Thus, the FePt nanoparticles hold great potential to serve as CT and MRI dual modality contrast agent.

Selective in Vitro Dual Modality Targeting Molecular Imaging of Her2/Neu. Further in vitro experiment demonstrated the binding specificity and MR contrast enhancement of antibody-conjugated FePt nanoparticles. The conjugation of anti-Her2 anitbody onto the FePt nanoparticles (FePt−anti-Her2) was achieved by the reaction of $-NH_2$ group of cysteamine on the nanoparticle surface with −COOH group of the antibody MBT2 cell with Her2/neu knock-down (MBT-KD) and the wild-type cell (MBT2) was used as the cell model. Figure 6a presented the T_2* weighted images of cell pellets after dosing of 3 nm-FePt, 3 nm-FePt−anti-Her2, 12 nm-FePt, and 12 nm-FePt−anti-Her2 with the same concentration (1 mM Fe), respectively. The quantitative results normalized to the signal intensity of the background were plotted in Figure 6b. For 3 nm-FePt, the signal intensities of the cell pellets showed minor signal reduction (3.6%) for the MBT-KD, while a 42% reduction in MR signal was observed in the MBT2 suggesting modulation of Her2/neu expression may have certain effect on the nonspecific uptake activity of 3 nm-FePt. On the other hand, both MBT-KD and MBT2 cells showed about equal signal intensity reduction when targeted by 12 nm-FePt (47.6% for MBT-KD and 49.7% for MBT2) suggesting nonspecific uptake of 12 nm-FePt was not significantly affected by the Her2/neu expression. In contrast, both 3 nm-FePt-anti-Her2 and 12 nm-FePt-anti-Her2 presented a significant Her2/neu expression-dependent signal reduction. A drastic reduction in MRI signal intensity (73.7% for 3 nm-FePt−anti-Her2 and 65.0% for 12 nm-FePt−anti-Her2) was observed when comparing the MRI signal of the MBT2 to that of the Her2 knock-down line MBT-KD. The cysteamine on these FePt nanoparticles could enhance the effect of cellar uptake and endocytosis.[50,51] On the other hand, the appreciable differences in the targeting nanoparticles conjugated with anti-Her2 antibody demonstrated the selectivity for Her2/neu high expression cells. Most worthily, 12 nm-FePt−anti-Her2 exerted the best MR contrast due to their higher magnetic susceptibility.

For the molecular CT imaging, we observed a significant effect of the particle size to the targeting contrast enhancement (Figure 6c,d). Although a 3.3 times (3.3×) positive contrast enhancement was observed in MBT2 compared to MBT-KD, the overall CT intensity was low in all test samples compared to 12 nm-FePt particles. CT contrast enhancement was observed in both MBT-KD (7.7×) and MBT2 (3.1×) targeted by 12 nm-FePt. The 12 nm-FePt−anti-Her2 successfully differentiates Her2-overexpressed wild-type cells (MBT2) from the gene knock-down line (MBT-KD) where a 3.1× signal intensity enhancement was detected. These results suggest the great potential for the 12 nm-FePt−anti-Her2 as a dual modality targeting molecular imaging contrast agent in MRI (inverse contrast) and CT (positive contrast).

(49) Jun, Y. W.; Huh, Y. M.; Choi, J. S.; Lee, J. H.; Song, H. T.; Kim, S.; Yoon, S.; Kim, K. S.; Shin, J. S.; Suh, J. S.; Cheon, J. *J. Am. Chem. Soc.* **2005**, *127*, 5732–5733.

(50) Mailander, V.; Landfester, K. *Biomacromolecules* **2009**, *10*, 2379–2400.

(51) Martin, A. L.; Bernas, L. M.; Rutt, B. K.; Foster, P. J.; Gillies, E. R. *Bioconjugate Chem.* **2008**, *19*, 2375–2384.

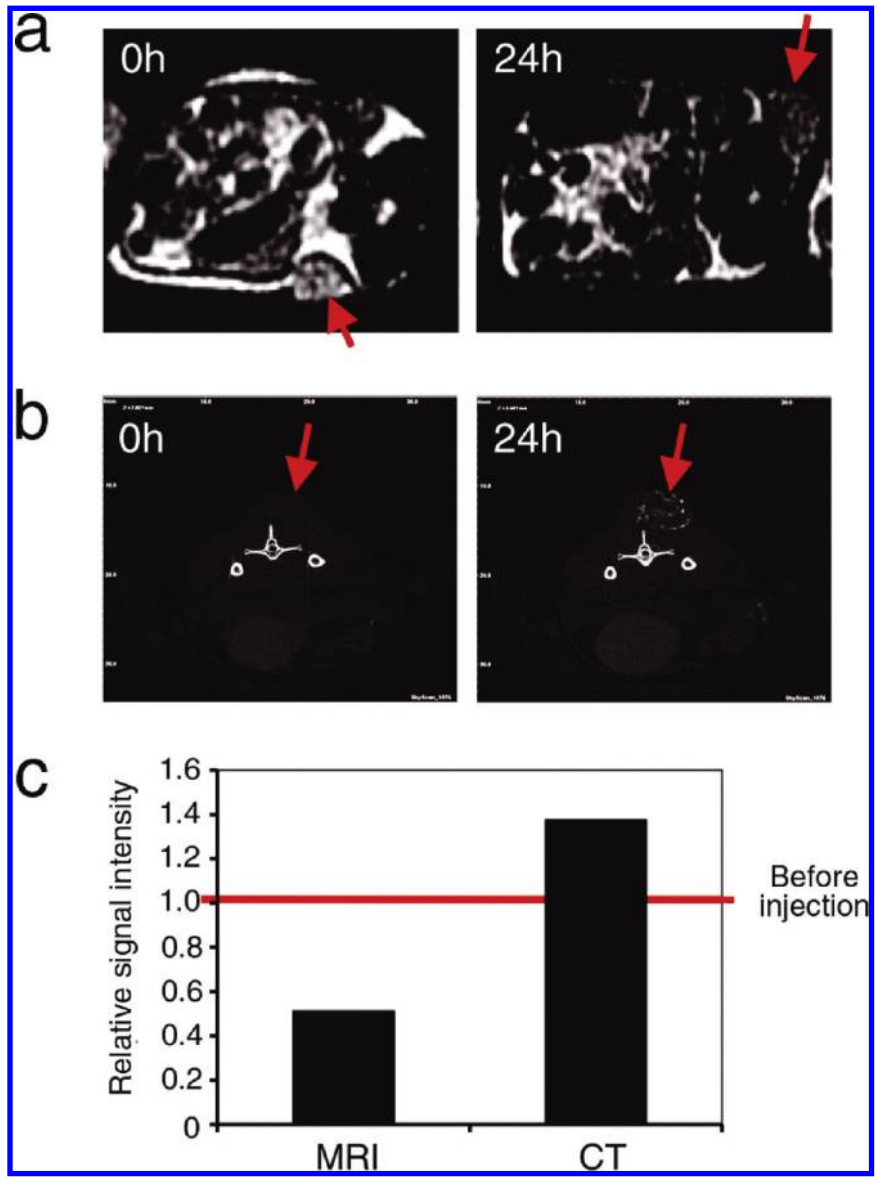

Figure 7. (a) Three-dimensional T_2*-weighted MR images of the mice bearing transplanted MBT2 tumor (as indicated by arrow) following tail vein injection of 12 nm-FePt−anti-Her2 obtained at 0 h (before injection, left panel) and 24 h after injection (right panel), respectively. (b) The CT images of the mice bearing transplanted MBT2 tumor (as indicated by arrow) was taken before (left panel) and 24 h after injection (right panel), respectively. (c) The alterations of the acquired image signal intensity after iv injection of the contrast agent in the tumor area under both MRI and CT is illustrated.

In Vivo Targeting Molecular Imaging of CT and MRI. The in vivo molecular imaging was performed in mice bearing transplanted MBT2 tumor. The 12 nm-FePt (28 mM Fe concentration, 100 μL) conjugated to the anti-Her2 monoclonal antibody was injected into mice through tail vein. The MR images were acquired before (0 h) and 24 h after injection (24 h) as illustrated in Figure 7a. The positions of tumor indicated by arrow were analyzed quantitatively. With respects to the MR images at time 0, a significant reduction of tumor lesion intensity to 51% was observed at 24 h after injection (Figure 7a,c). On the other hand, a significant 138% contrast enhancement of the tumor tissue 24 h after targeting was observed in CT image analysis (Figure 7b,c). These in vivo experiments showed that the anti-Her2 conjugated FePt nanoparticles selectively target Her2/neu overexpressed tumor lesions after systemic administration and are sufficient to contrast the Her2 expression in tumor lesions using both T_2* MRI sequence and CT modalities.

Taking together the in vivo molecular targeting MRI and CT results, the as prepared 12 nm-FePt−anti-Her2 presents a great potential as the dual modality molecular imaging contrast agent that may combine the advantage of radiofrequency induced hyperthermia for therapeutics in future developments.

Conclusions

In conclusion, the biocompatible FePt nanoparticles with tunable sizes were prepared by a simple method. The in vitro MR images and CT scans demonstrated that the alloy FePt nanoparticles could serve as a dual modality contrast agent for CT/MRI molecular imaging. The surface chemistry of the alloy nanoparticle enabled simple conjugation to mono-

clonal antibody and other function ligands. This property further extends their in vivo applications as CT/MR dual modality molecular imaging contrast agents. The in vivo dual modality molecular imaging capability was successfully confirmed by targeting Her2/neu oncogene expression in cancer lesions in mice using monoclonal antibody conjugated FePt nanoparticles. In addition, the biodistribution of the three sizes of FePt nanoparticles suggest that all these particles could be cleared from the body after about 1 week. The 12 nm-FePt presented the highest serum concentration and circulation half-life as well as the highest image contrast effect in both CT and MRI. The 3 nm-FePt presented the highest plateau concentration in the brain and is ideal for future multimodal brain imaging. Combined with the potential for radiofrequency-induced hyperthermia, this nanoparticle also holds great potential for future theranostic platform.

Acknowledgment. We thank National Science Council of Taiwan for supporting this project under grant 98-2218-E-006-008-MY3, 98-3114-M-006-002, and 98-3114-M-003-001.

Supporting Information Available: FTIR spectra as mentioned in this report. This material is available free of charge via the Internet at http://pubs.acs.org.

JA1035013